INTERNATIONAL JOURNAL OF ARCHITECTURAL HERITAGE
https://doi.org/10.1080/15583058.2025.2565241

RESEARCH ARTICLE

Experimental Study of Combustion and Upward Flame Spread Characteristics of Accelerated Weathered Pine

Kai Wang[a], Danping Hao[a], Xuyao Wang[a], Chenyang Jiang[a], Yoshioka Hideki[b], Muying Ge[a], Xuan Wang[c], and Biao Zhou[a]

[a]School of Emergency Management and Safety Engineering, China University of Mining & Technology (Beijing), Beijing, China; [b]Department of Architecture, Faculty of Engineering, University of Tokyo, Tokyo, Japan; [c]School of Civil and Environmental Engineering, Ningbo University, Ningbo, China

ABSTRACT

Wooden structures are vital to global cultural heritage. Recent fires have caused irreversible losses. Vertical upward flame propagation characteristics of pine wood with varying grain directions under artificial accelerated weathering cycles were examined. Material properties, combustion phenomena, flame height, wall heat flux density and propagation rate were studied. A pine weathering vertical wall flame propagation model was developed via dimensionless analysis. Results showed non-monotonic changes in wall temperature and heat flux with weathering cycles. Flame temperatures for grain-aligned pine exhibited secondary peaks. Flame height oscillated periodically due to entrainment. After 35 cycles, flame height reached 700–900 mm, peak heat flux was 30 kW/m^2, and the time to ignition (TTI) decreased by 68% after initial cycles. Increased weathering caused long-term low-frequency flame height jitters with smaller secondary peaks. Critically, a new weathering coefficient model for flame prediction was established, and the bimodal temperature phenomenon in vertical-grain pine was confirmed, advancing heritage building fire safety. Pine grain direction significantly impacted flame height, while propagation rate demonstrated complex dependencies on weathering cycles, wall heat flux, and flame height. These insights optimize ancient building fire protection strategies.

HIGHLIGHTS

- A novel vertical flame spread model integrates weathering cycles and wood grain in pine combustion dynamics.
- Flame height exhibits dual-peak oscillations linked to weathering-induced volatile release and air entrainment effects.
- Vertical-grain pine yields larger carbonization zones, while horizontal-grain accelerates horizontal flame propagation.
- The weathering coefficient quantifies flame spread dependencies on heat flux, cycle duration, and anisotropic shrinkage.
- Experimental validation confirms non-monotonic heat flux trends and flame jitter in weathered pine walls.

ARTICLE HISTORY
Received 3 May 2025
Accepted 19 September 2025

KEYWORDS
Flame height; upward flame spread; weathered wood; weathering cycles; wooden cultural heritage

1. Introduction

As a carrier of civilization, historical buildings have important cultural, scientific, and aesthetic values and carry the historical memory and artistic achievements of human society (Zhou, Jiang, et al. 2024). However, their unique wooden structure characteristics, the current situation of long-term exposure to the outdoor environment, and complex building structures and ventilation conditions make them face severe fire risks, which pose a major challenge to cultural relic protection (Kránitz et al. 2016a; Yi et al. 2024). In recent years, historical building fires have occurred in Brazil (Sá, Sá, and Lima 2018), France (Mackie and Sim 2019), the United Kingdom, Japan, and other places, causing irreversible losses. Long-term weathering significantly deteriorates wood, accelerating flame spread and making fires harder to control, resulting in irreversible damage to cultural relics and heritage (Zhou et al. 2019). The spread of flame on the surface of wood is complex (Popescu and Pfriem 2020; Xu et al. 2024). Compared with fresh wood, weathered wood may be more dangerous in terms of fire safety (Song et al. 2022; Xu et al. 2020). Weathering-induced porosity increase and cellulose degradation elevate fire risks through enhanced volatile release (Di Blasi

CONTACT Biao Zhou ✉ zhoubiao1088@gmail.com; zhoubiao1088@bme.arch.t.u-tokyo.ac.jp 🖃 School of Emergency Management and Safety Engineering, China University of Mining & Technology, No.11 Xueyuan Road Street, Haidian District, Beijing 100083, P.R. China

2008; Srinivas and Pandey 2012). Despite extensive research on the fire behavior of continuous wood, there is still no thorough understanding of vertical wall flame spread in weathered wood.

Numerous studies have sought to model the dynamics of vertical flame spread. Most existing fire plume theories are rooted in an axisymmetric framework, concentrating on factors influencing flame height and its dimensionless characterization (Delichatsios 1993; Heskestad 1998; Heskestad 2016), fire plume theoretical model construction (Morton, Taylor, and Turner 1956; Rouse, Yih, and Humphreys 1952; Schmidt 1941), the flame spread models for hot thick solids (Atreya, Carpentier, and Harkleroad 1986; Hasemi 1984; Heskestad 1999) and binary contrast of fresh and weathered wood (Hartikainen et al. 2018). Although some research has delved into the vertical flame spread of weathered wood, the effects of wood grain orientation and weathering cycles remain understudied (Hu et al. 2024). Furthermore, prevailing investigations predominantly examine traditional wood samples, neglecting the critical effects of weathering. While prior work has advanced understanding of horizontal flame spread under the influence of environmental factors (Chen et al. 2023), material thickness (Ma et al. 2021) and density (Zhou, Zhou, et al. 2024), research on vertical flame spread of weathered wood remains a critical gap. Given the significant losses of historic buildings to fire, investigating the effect of weathering degree on vertical flame spread of wood would bridge this gap, providing essential insights into fire dynamics of weathered wooden structures and improving fire risk assessment in practical engineering.

To further elucidate the influence of weathering processes on vertical flame spread behavior, this study conducts a series of tests to systematically examine the mass loss, dimensional shrinkage, wall heat flux density, flame height, charred area and flame spread rate of pine wood samples in both fresh and weathered states. By controlling weathering cycles to quantify the patterns of wood weathering and integrating these findings with microstructural characterization, the theoretical model is refined. This work examines variations in wall heat flux density related to sample texture and weathering cycles, proposing an explanation for how weathering influences vertical flame spread over pine wood.

2. Materials and methods

2.1. Materials

Material selection in traditional Chinese timber architecture prioritizes the use of locally available materials. Coniferous species from the Pinaceae family, particularly Pinus sylvestris var. mongolica, have become predominant construction materials in northern and northwestern China, specifically in Shanxi, Hebei, and Inner Mongolia. These species offer an optimal balance between mechanical performance and economic viability, serving primarily in non-critical structural components. With the decline in availability of high-quality hardwoods, fast-growing pine species have gained prominence in heritage conservation due to their sustainable supply chain. This operational significance informed our experimental selection of pine specimens for accelerated weathering analysis, as illustrated in Figure 1.

Before the accelerated weathering experiments, all specimens were equilibrated in a climate-controlled chamber at 23 ± 2°C and 50 ± 5% relative humidity for 60 hr. Baseline measurements of dimensions and mass were systematically recorded after material properties stabilized, defined as <0.1% variation in mass over three consecutive hourly measurements.

2.2. Accelerated weathering test methods

Accelerated weathering protocols were designed to simulate multi-factor degradation processes in historical timber structures. Pine samples were treated with water spraying, UV exposure and alternating high and low temperatures to assess the impacts of humidity, temperature and UV exposure. The weathering process is shown in Figure 2, with each cycle comprising 4 hr of water spraying, 4 hr of UV exposure, 4 hr of drying at 60°C and 4 hr of low-temperature exposure at −20°C, totalling 12 hr per cycle. The number of cycles executed includes 0, 7, 14, 21, 28, 35, 42 and 49.

During the water spraying phase, purified water is uniformly applied to the surface of the samples using

Figure 1. Fresh pine samples. (a) vertical grain (b) horizontal grain.

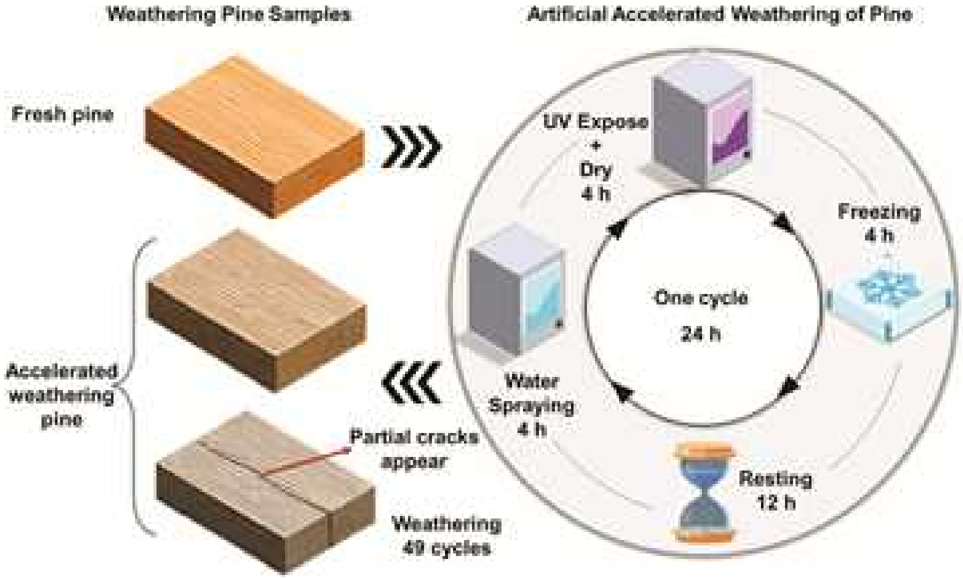

Figure 2. The illustration of the weathering process configuration.

a nozzle, with the positions of the samples rotated in each cycle to ensure consistent water exposure. Ambient temperature is maintained between 16°C and 25°C, with relative humidity set at ≥70%. In the UV exposure and drying stages, the irradiation intensity is calibrated to 1.55 W/(m^2 ·nm), with a blackboard temperature of 60°C and relative humidity controlled between 45% and 70%. Before conducting the flame spread test, the pine samples were conditioned in a constant temperature and humidity environment for 96 hr, achieving a moisture content of approximately 20.0 ± 0.5% (Zhou et al. 2022).

2.3. *Visual and microscopic evaluation*

Surface changes were analyzed utilizing a 1100× magnification cold-field emission high-resolution scanning electron microscope (HITACHI FESEM SU8100, Hitachi High-Technologies, Japan).

Dimensional measurements of pine specimens, including length (L), width (W) and thickness (R) of both the front and back surfaces, were recorded pre- and post-accelerated weathering using calipers. Measurements were taken twice at each extremity and along the centerline, and averaged to an accuracy of 0.1 mm. The shrinkage (Δd) was employed to quantify the dimensional changes experienced by the pine as a result of the accelerated weathering process.

$$\Delta \mathrm{d} = \frac{\mathrm{d} - \mathrm{d}_0}{\mathrm{d}_0} \times 100\% \tag{1}$$

where d_0 is the initial size and d is the size after accelerated weathering. If the sample is warped, the distance between the ends is still measured, and the bending length is not measured.

2.4. *Cone calorimeter analysis*

Pine samples were subjected to combustion testing using the FTT iCone2+ cone calorimeter (Fire Testing Technology Ltd.), following ISO 5660 standards, applying a thermal radiation flux of 50 kW/m^2. Each sample measured 100 × 100 × 20 mm and was left undisturbed for 50 hr, wrapped in tin foil with the upper surface exposed.

The cone calorimeter generates a controlled fire environment by delivering a constant external heat flux. Time to ignition (TTI) is recorded when the surface temperature of the pine reaches its critical ignition threshold. Under ideal conditions, disregarding convection and radiation losses and modelling the sample as a one-dimensional semi-infinite solid, TTI can be expressed as follows:

$$\mathrm{TTI} = \frac{\pi}{4} \cdot \frac{k_s \rho_s c_s}{\left(q''_{ext} - q''_{crit}\right)^2} \tag{2}$$

where k_s is the thermal conductivity of pine, W/(m·K); ρ_s is the density of pine, kg/m^3; c_s is the specific heat capacity of pine, J/(kg·K); q_{ext}'' is the applied external heat flux, kW/m^2; q_{crit}'' is the critical heat flux of pine wood, kW/m^2. According to the heat balance theory, when the heat absorbed by the surface of pine wood is sufficient to raise the temperature to the critical value, ignition occurs. At this time, the ignition temperature can be derived through the heat conduction theory:

$$T_{\mathrm{ig}} = T_\infty + q''_{ext}\sqrt{\frac{4TTI}{\pi k_s \rho_s c_s}} \tag{3}$$

where T_∞ is initial ambient temperature, K.

2.5. Experimental setup

After each accelerated weathering cycle, ignition and flame propagation test samples were prepared, measuring $284 \times 284 \times 20$ mm $(L \times T \times R)$. n-heptane was utilized to create flame exposure. Following the research methods of Hasemi, a bespoke vertical flame propagation experimental platform was constructed, as illustrated in Figure 3 (Hasemi 1984). This platform comprises an embedded wall body measurement device, an ignition mechanism, and a supporting structure, effectively simulating ignition and fire conditions on building facades. The experiments were conducted under ambient temperature and pressure conditions, with each trial repeated in triplicate. The entire experimental procedure was recorded using a digital camcorder. Flame spread data were subsequently extracted through systematic video analysis.

Before the experiment, the specimen was conditioned at 10°C and 35% relative humidity for 48 hr. During testing, high-temperature resistant aluminum foil was employed to encase the five sides of the specimen, leaving only the front side exposed, ensuring that flames were generated and spread exclusively on this surface. The vertical wall temperature and heat flux were continuously monitored by K-type thermocouples and heat flux sensors until the surface of the pine sample was fully consumed or extinguished. Subsequently, the camera was turned off. K-type thermocouples (accuracy ±1.5°C) were calibrated using ice-water (0°C) and boiling water (100°C) benchmarks before each test, following ASTM E230–25.

3. Physical observation

3.1. Combustion phenomenon

Burning duration for pine is detailed in Table 1 and Figure 4, defined as the interval between ignition onset and complete fuel consumption. Vertical flame propagation exhibited four stages: (I) ignition initiation, (II) pyrolysis front progression, (III) steady combustion and (Ⅳ) flame recession. Each stage showed distinct flame-height profiles and combustion characteristics. Thermal degradation initiated at the pine base, releasing combustible volatiles. Vertical propagation accelerated after surface char layer formation, progressing preferentially along axial tracheids. This created an extended preheating zone, with flame fronts maintaining acute angles to the surface; oxygen diffusion along fibers sustained stabilized premixed combustion (Quintiere, Margaret, and Hasemi 1986). Stage III culminated in clustered combustion patterns, with simultaneous base charring and flame-height reduction. Weathering-induced structural modifications (e.g., tracheid collapse from volatile transport obstruction) promoted intermittent flame stratification and buoyancy-driven convective reignition.

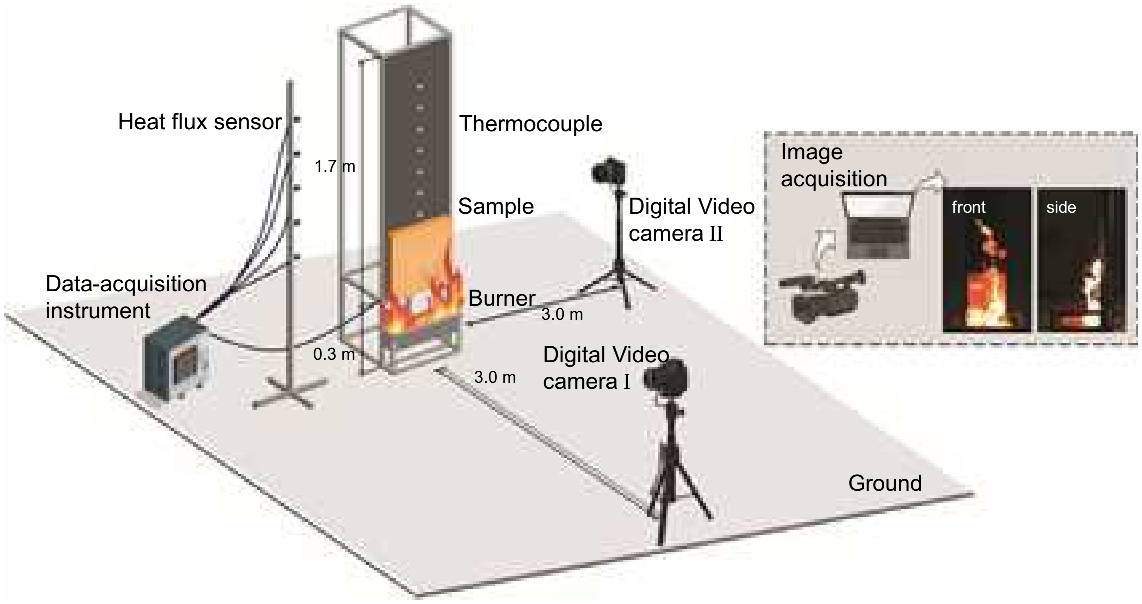

Figure 3. Experimental setup.

Table 1. The description of flame spread time for different grains of wood in each weathering cycles.

Test No.	Weathering or not	Woodgrain	Weathering cycles	TTI (s)	Development stage time (s)	Continuous burning time (s)	CAR (%)
1	NO	Vertical	0	78	17	117	72.9
2	YES	Vertical	7	191	16	84	61.0
3	YES	Vertical	14	121	14	83	90.3
4	YES	Vertical	21	185	14	80	71.8
5	YES	Vertical	28	176	11	98	80.8
6	YES	Vertical	35	56	33	154	89.3
7	YES	Vertical	42	35	10	153	92.4
8	YES	Vertical	49	140	10	119	93.1
9	NO	Horizontal	0	59	20	226	92.7
10	YES	Horizontal	7	168	15	71	66.9
11	YES	Horizontal	14	45	16	138	77.1
12	YES	Horizontal	21	160	14	179	69.1
13	YES	Horizontal	28	39	20	147	63.4
14	YES	Horizontal	35	57	25	167	57.5
15	YES	Horizontal	42	35	10	153	72.6
16	YES	Horizontal	49	60	9	95	70.2

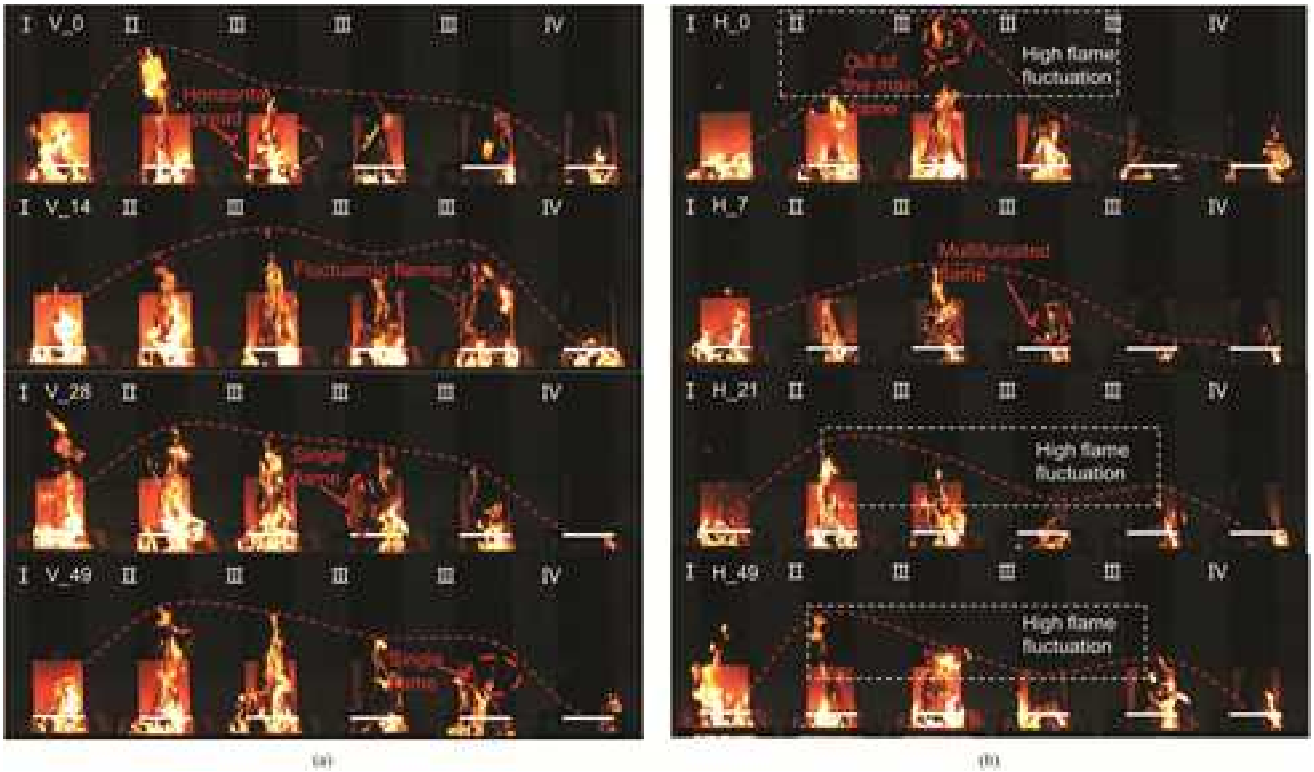

Figure 4. Typical transient flame images under different weathering cycles and grain (V or H) conditions. (a) vertical grain pine with fresh and weathering for 14, 28 and 49 cycles (b) horizontal grain pine with fresh and weathering for 7, 21 and 49 cycles.

Horizontal combustion showed increased flame spacing, reduced fusion, and gaps between the flame base and surface. Restricted lateral heat transfer and oxygen diffusion resistance prolonged oxidizer paths, yielding incomplete premixing and dispersed flames with enhanced particulate emission (Zhou et al. 2021).

Vertically grained pine showed nonlinear TTI dependence on weathering severity. It increased by 1.5 times due to fiber shrinkage and microcrack heat dissipation. During the middle and late stages, reduced ignition thresholds from crack propagation and hemicellulose depolymerization shortened TTI, followed by a resurgence in ignition delay driven by porous structural heat dispersion (Wang et al. 2024). Vertical flame kinetics correlated with char layer evolution, initial acceleration via axial thermal conductivity enhancement, mid-weathering suppression from char densification and late reactivation via pyrolysis front destabilization. Sustained combustion duration decreased by 43.9% early due to char compaction, rebounded mid-late via chain-reaction volatile release, then declined terminally from structural failure. Horizontally grained weathered pines showed a 1.9 times TTI increase early, stabilizing at approximately 50-s mid-late due to porosity. The pyrolysis front progression stabilized at 30 s, reflecting heat loss–inertia balance. It is worth noting that flame height and spread rate were averaged over time during periods of stable flame propagation.

3.2. Carbonized area changes with weathering cycles

Wood grain and weathering affect pyrolysis and combustion. Comparing area ratio (CAR), defined as residual carbonized material proportional to the initial exposed area, showed grain-dependent responses. Table 1 presents the surface carbonization results for vertical and horizontal grain pine after 0 to 49 weathering cycles in the vertical flame experiment.

Comparative analysis indicated 20% CAR elevation in vertically grained pine versus fresh wood after 28 weathering cycles, contrasting with 68.17% average CAR reduction in weathered horizontal-grain specimens. Early weathering (cycles 0–28) CAR variability correlated with compositional shifts, and hemicellulose degradation amplified cellulose-lignin dominance. Subsequent combustion efficiency improved through diminished volatile emission, stabilizing CAR values exceeding fresh controls by 20%. Stable char-layer retention yielded shallow combustion zones with grayish-white ash. Horizontal grains showed structural degradation, increasing convective heat losses and disrupting flame-oxygen mixing and reducing surface carbonization. Grain-aligned combustion intensified kinetics, and transverse combustion faced cellular resistance. Progressive cycles accentuated CAR divergence, highlighting grain-dependent flame regulation.

3.3. Wall temperature changes with weathering cycles

Temperature characterizes material combustion and flame propagation, capturing weathering and grain effects. Figure 5 shows the temporal evolution of terminal pine temperature across weathering cycles, from n-heptane ignition to fuel burnout.

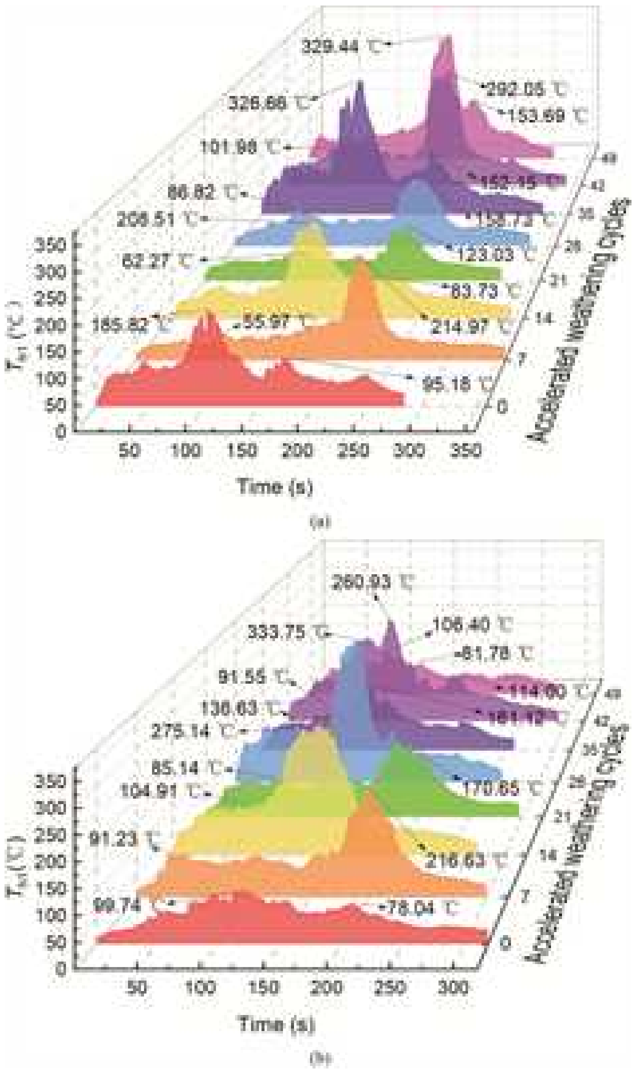

Figure 5. Terminal temperature of pine fuel with time in different weathering cycles. (a) vertical grain pine (b) horizontal grain pine.

Fresh vertical-grain pine peaked at 185.82°C. With 7 to 14 cycles, the temperature peak magnitude and concentration increased and the heating rate accelerated as hemicellulose decomposition released volatiles. Cycles 21 to 28 reduced peak temperature below fresh pine due to hemicellulose degradation, limiting volatile release and shortening flame duration. As weathering progresses, peak temperatures can reach 300°C, with extended durations above 250°C and an earlier 150°C secondary peak, indicating pine structural weakening.

Horizontal-grain pine showed prolonged combustion but reduced peak temperature. The peak temperature in horizontal grain pine occurs later, and a secondary peak emerges after a prolonged interval. This behavior is attributed to the horizontal pores, which facilitate heat conduction but simultaneously enhance convective heat dissipation, leading to reduced peak temperatures and moderated flame spread, thus causing fluctuations in temperature. Flame spread primarily horizontally, causing local reignition post-vertical cessation.

4. Results and discussion

4.1. Material properties

4.1.1. Dimensional shrinkage

Wood hygroscopicity is linked to dimensional stability. Weathering reduces moisture absorption, impairing performance. Humidity and temperature fluctuations cause rapid pine expansion and contraction. During accelerated weathering, pine exhibited anisotropic expansion and longitudinal changes were minimal, below 0.4%, indicating microfibril alignment stabilizing dimensions. Abnormal contraction at 21 cycles may stem from cellulose chain contraction at high temperatures.

The observation was carried out at an acceleration voltage of 3 kV with a magnification of 1,100 times, and the working distance was 15.8–16.0 mm. Perpendicular to the grain, expansion escalates incrementally, highlighting the material's sensitivity to wet-heat cycles. The average expansion rate over 7 to 49 cycles is 2.14%, driven by ultraviolet-induced lignin degradation and hemicellulose hydrolysis prompted by wet-heat cycles (Kropat, Hubbe, and Laleicke 2020). Early weathering (7 to 21 cycles) showed pronounced dimensional fluctuations from lignin photooxidation. As Figure 6 shows, photodegradation primarily affected the pine surface, with intercellular layers exhibiting higher lignin concentrations than the cell walls. Later stages (28 to 49 cycles) showed dimension stabilization from hemicellulose hydrolysis (Hon and Feist 1986; Tolvaj and Faix 1995). Heat treatment exacerbated dimensional changes, alternating cold-heat cycles degraded hemicellulose sugar branches into low-molecular-weight soluble substances, reducing moisture-absorbing groups. High-crystallinity cellulose and condensed lignin diminished ductility.

A two-way anomaly after 49 cycles showed a 45% vertical grain width increase and a 4.8% horizontal grain thickness decrease, correlating with cellulose crystalline region reconstruction and microcrack shrinkage (Obataya 2012), causing irreversible cell cavity collapse. Figures 7 and 8 demonstrate that during the initial four weathering cycles, wood primarily absorbed moisture and expanded, with the horizontal grain length difference reaching 1.525 mm. In contrast, the final three cycles revealed morphological instability due to microstructural damage. As a result, the ratio of width to thickness differences in the vertical grain of the pine sample diminished from 5.12 at 7 cycles to 1.15 at 49 cycles, highlighting a significant weakening of its anisotropic characteristics.

4.1.2. Mass loss

The mass change in pine during weathering depended on water spray, high-temperature pyrolysis and UV irradiation. Pyrolysis can be quantitatively assessed by measuring the mass loss before and after heat treatment. Following artificial accelerated weathering, the sample is conditioned for over 50 hr at a relative humidity of 50 ± 3% and a temperature of 23 ± 2°C to achieve equilibrium. Once mass stabilization is confirmed, four measurements are taken using a precision balance with 0.01 g accuracy, and the arithmetic mean is calculated. The mass loss rate (MLR) is then determined using the following method:

$$\mathrm{MLR} = \frac{m - m_0}{m_0} \times 100\% \tag{4}$$

where m_0 is the initial mass of the sample, and m is the mass of the sample after accelerated weathering.

Figure 9 depicts mass and MLR changes. As a porous material, wood contains free water within its cell cavities and bound water in its cell walls (Kropat, Hubbe, and Laleicke 2020), with mass alterations linked to moisture absorption. In the initial three cycles, the MLR increased

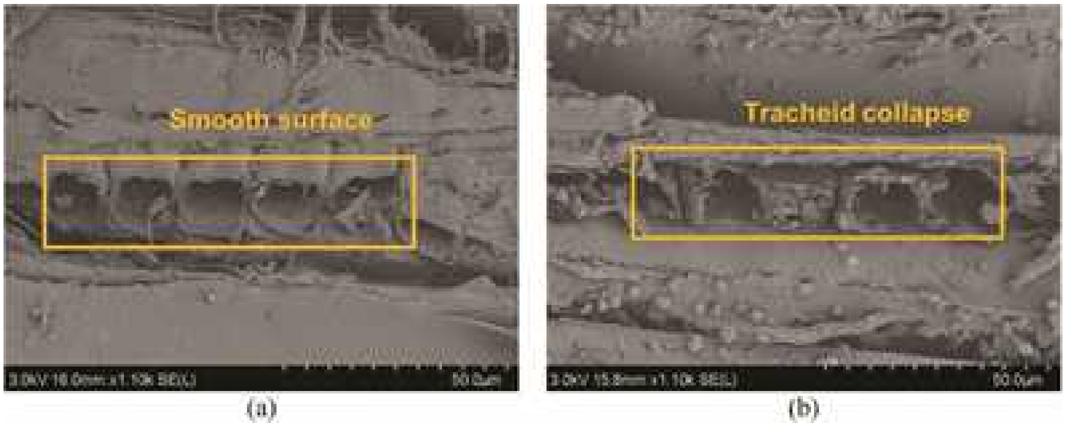

Figure 6. SEM results of the experimental samples (false-colored). (a) fresh pine sample (b) accelerated weathering 49 cycles pine.

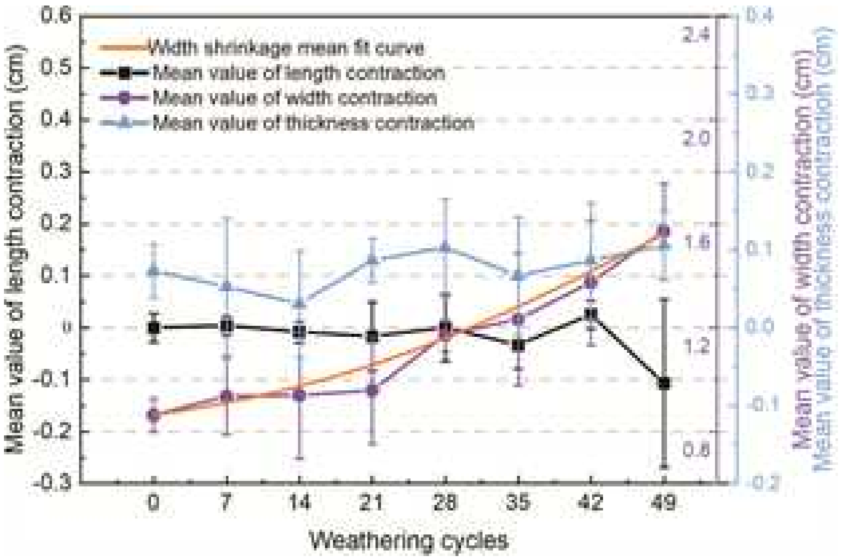

Figure 7. Size change of pine with the accelerated weathering cycles.

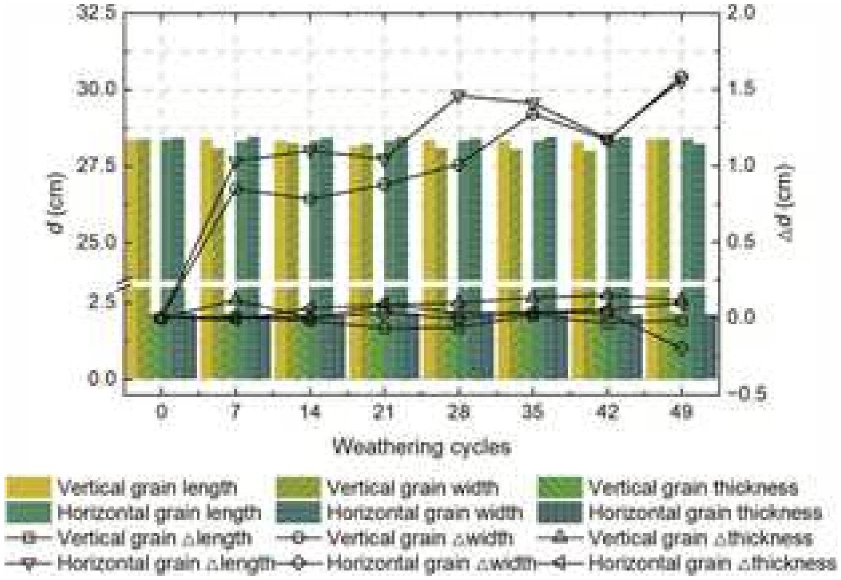

Figure 8. Dimensional changes in pine with different accelerated weathering cycles.

from 7% to 10%, and higher initial mass samples showed greater susceptibility. Early mass change is driven by heat treatment and humidity cycling. Cellulose resisted hydrolysis but facilitated moisture penetration through its expansive surface area. In contrast, hydrophilic hemicellulose degraded under heat, humidity and UV. Hemicellulose leaching inhibited moisture absorption (Herrera et al. 2018).

Later weathering stabilized the mass loss and MLR between 10% and 13%. Mass changes are primarily affected by water spraying scouring. UV radiation oxidized lignin, depolymerizing it into aromatics and acids. Hemicellulose leaching extracted inorganics, enhancing porosity and pore diameter (Kránitz et al. 2016b). Medullary ray cracks expanded from temperature-humidity cycles, accelerating internal weathering and surface delamination. These mechanisms caused characteristic surface peeling and erosion (Žlahtič Zupanc and Humar 2016).

4.2. *Ignition of weathered pine*

Under typical fire conditions, solid materials undergo heating, resulting in the release of combustible gaseous pyrolysis products. These gases diffuse through natural convection and turbulence, filling the boundary layer

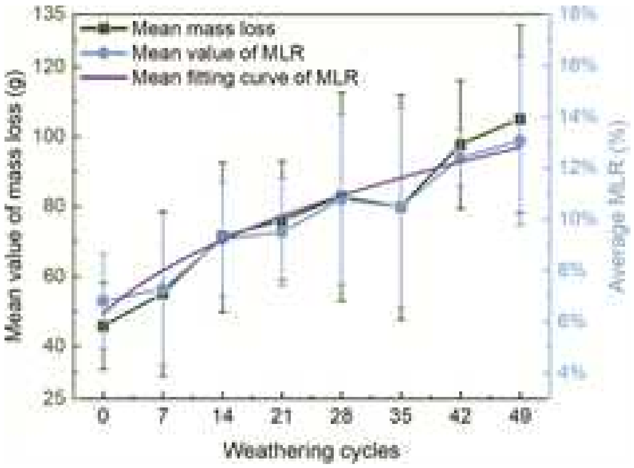

Figure 9. Mass loss and MLR as a function of weathering cycles.

and mixing with ambient air. This process is accompanied by a continuous increase in surface temperature until it reaches a threshold that can sustain ignition. At this point, the combustible material enters a state of "thermal runaway," triggering a chemical reaction that leads to combustion. Consequently, the TTI for weathered pine can be characterized as the cumulative duration necessary for: conduction heating to elevate the solids to their pyrolysis temperature, the concentration of combustible gases and oxygen to reach levels sufficient to support a small, sustained fire and the ignition of the flammable mixture to maintain combustion (Gorbett and Kozhumal 2023).

In instances of piloted ignition, the timescales for chemical reactions and fuel-air mixing are sufficiently brief, allowing the TTI to be approximated by the duration required for heat transfer to elevate weathered pine to its pyrolysis temperature. Table 2 illustrates a consistent decrease in the TTI of weathered pine. The T_{ig} for both fresh and weathered pine exhibited a non-monotonic decreasing trend, initially decreasing by 68% over the first three cycles, followed by a reduction to approximately 23% of the fresh T_{ig} in the last four cycles, culminating in a minimum TTI of 14 s after 35 cycles. The rapid decrease in TTI during the first 14 cycles is attributed to lignin decomposition, which enhances the production of volatile compounds and accelerates the pyrolysis rate. Conversely, between cycles 14 and 35, variations in hygroscopicity and pore structure reorganization contributed to oscillations in TTI. The formation of a carbonized layer in the later stages of weathering also impedes oxygen diffusion.

Moisture content emerged as a critical factor influencing ignition performance; pine with high moisture content requires prior evaporation of water, which absorbs heat and prolongs the TTI. Furthermore, T_{ig} exhibited a non-monotonic trend post-weathering, initially increasing by 6.1% in the first three cycles before decreasing in the last four to around 17.4% of the fresh T_{ig}. As weathering progresses, moisture depletion and the pyrolysis of hemicellulose in the initial cycles lead to a reduction in volatile products. This pyrolysis process shifts to higher temperatures for cellulose and lignin, while hemicellulose undergoes nearly complete degradation in subsequent cycles. Consequently, the moisture adsorption capacity diminishes, leading to a loosely packed microstructure in the pine. Thus, the weathering coefficient of pine can be formulated as:

$$\Pi = \frac{\frac{\Delta \mathrm{d}}{d_0} \times \frac{S_i}{S_0}}{\frac{\Delta \mathrm{m}}{m_0}} \tag{5}$$

where $\frac{d}{d}$ is the size shrinkage ratio. d is the dimensional shrinkage difference in the vertical grain after weathering, cm. d_0 is the horizontal length of pine before weathering, cm. The ratio of the two is a dimensionless parameter that can directly reflect the structural degradation, such as increased porosity and reduced fiber crystallinity. $\frac{m}{m}$ is the mass difference ratio.

Table 2. Sample TTI and T_{ig} for each weathering cycle.

Weathering cycles	0	7	14	21	28	35	42	49
TTI	66	60	21	24	17	14	17	15
T_{ig}	405.6	412.4	424.3	430.4	363.5	347.5	323.1	335.1

Δm is the mass loss value of pine after weathering, g. It is a dimensionless parameter and is related to the deterioration of pine hygroscopicity, chemical degradation, or release of volatile components. $\frac{S_i}{S}$ is the CAR. S_i is the surface carbonization area of a single-textured weathered pine after combustion, cm^2. S_0 is the initial surface area of the sample, cm^2. The ratio of the two changes with grain factors and weathering cycles. i is the weathering cycle number.

The three parameters delineate chemical changes, physical deformation and mass loss characteristics, addressing distinct dimensions of vertical and horizontal grain pine during weathering and combustion. Given their independent operation, reliance on any single parameter does not suffice to capture the complexities of chemical degradation, structural alterations, mass loss and shifts in combustion mechanisms. Therefore, integrating these parameters provides a comprehensive quantification of the multifaceted effects of artificial pine weathering. Given the varied numerical ranges of the parameters, a simple additive approach fails to accurately represent their interactions. Instead, a combination of ratio and product formats is employed. The size shrinkage ratio effectively amplifies the influence of chemical changes, while the mass difference ratio in the denominator mitigates the effects of physical property alterations caused by weathering. Furthermore, the CAR accounts for both grain orientation and weathering cycles, allowing the weathering coefficient to encapsulate the superficial characteristics imparted by artificial weathering and elucidate the variations in combustion dynamics and flame spread behavior resulting from these processes. In contrast, (Hartikainen et al. 2018) focused solely on mass loss, while Hasemi (Hasemi 1984) considered only heat flux boundary layer thickness, limiting their ability to quantify weathering-specific degradation.

4.3. *Flame height*

Flame height is a key parameter that reflects the characteristics of flame spread, influenced by factors, such as the fuel heat release rate, combustion radiation properties and fuel morphology. The flame is also subject to disturbances from its environment and oscillations induced by the coil suction effect, resulting in temporal variations in flame height. This behavior often leads to a gradual detachment from the main flame body, as illustrated in Figure 4 (Cetegen and Ahmed 1993). When flames propagate along grain surfaces, they typically reach a peak height of 700 to 800 mm with minimal oscillation amplitude. Weathering of pine extends the preheating zone and enhances the wall effect between the flame plume and the surface, which mitigates oscillation to some degree. Extended fuel heating elevates ambient temperatures, altering the air boundary layer and intensifying convective vortex effects. This can cause the flame tip and main body to delaminate and oscillate independently (Yan 2022).

In perpendicular grain propagation, the lateral spread prolongs combustion duration, allowing flame heights to peak between 700 mm and 900 mm. But diminishes the flame plume's influence on the pine surface. As a result, the flame front may intermittently detach from the wall, leading to heightened oscillation amplitude. Remarkably, even during the bottom-burning stage, once the flame reaches the top of the wood surface, it continues to exhibit substantial height fluctuations. In the later stages of combustion for weathered pine, particularly around 100 to 120 seconds, a sharp decline in flame height occurs, dropping below 200 mm. This decline is attributed to the cessation of vertical flame spread on the pine surface, resulting in a shift toward slower horizontal propagation. During the later combustion stages of wood weathered for 35 and 42 cycles, a smaller peak in flame height is observed. At 49 cycles, a gradual increase in flame height occurs with low-frequency fluctuations. Weathering-induced surface cracks give rise to multiple independent flame units, leading to the formation of single or multi-cluster flames in charred areas. These clusters compete for oxygen, creating combustion instability and fluctuations in flame height within a reduced range.

To further analyze the chemical processes within the flame reaction zone, we employ a linear fire source wall flame model. In this framework, we treat the chemical reaction process as a stable energy source within the energy equation, neglecting fuel diffusion and solid pyrolysis effects:

$$\rho \frac{\partial u}{\partial x} + \rho \frac{\partial v}{\partial y} = 0 \tag{6}$$

$$\rho \left(u \frac{\partial u}{\partial x} + v \frac{\partial v}{\partial y} \right) = g(\rho_\infty - \rho) + \frac{\partial}{\partial y} \left(\mu \frac{\partial u}{\partial y} \right) \tag{7}$$

$$\rho c_p \left(u \frac{\partial \theta}{\partial x} + v \frac{\partial \theta}{\partial y} \right) = \frac{\partial}{\partial y} \left(\lambda \frac{\partial \theta}{\partial y} \right) + \frac{\partial \dot{q}_r''}{\partial y} + \dot{q}''' \tag{8}$$

where u and v are the velocities in the x and y directions respectively, mm/s; g is the acceleration due to gravity, taken as 9.80 m/s^2; ρ_∞ is the environmental density, kg/m^3; c_p is the specific heat capacity, kJ/(kg·K); θ is the excess temperature, $\theta = T - T_\infty$, K; $\dot{q}_r''$ is the radiative heat flux, kW/m^2; is the energy released by chemical reaction, kW/m^2 .

Introduce the temperature field and velocity field to solve the integral equation:

$$\theta = \theta_1(x)G(\eta) \tag{9}$$

$$u = u_1(x)F(\eta) \tag{10}$$

where $\eta = \frac{z}{\delta(x)}$, $\delta(x)$ is the boundary layer thickness; $u_1 = u_0x^{\frac{1}{2}}$, $\theta_1 = \theta_0$, $\delta = \delta_0 x$.

It is assumed that the reaction zone ceases to exist once the fuel is fully consumed. The flame height is primarily influenced by the fuel supply rate, oxygen concentration and the entrainment rate of oxygen driven by buoyancy, which can be expressed as (Quintiere, Margaret, and Hasemi 1986):

$$\int_0^H Y_{\mathrm{Ox},\infty}(-\rho v)_{y\to\infty}dx = \varepsilon r\dot{m}' \tag{11}$$

where H is the flame height, mm; $Y_{Ox,\infty}$ is the mass fraction of oxygen in the environment; ε is the mixing coefficient, which depends on the flame fluid dynamics; r is the stoichiometric oxygen to fuel mass ratio; $\dot{m}'$ is the fuel supply rate. Following Liburdy and Faeth for the high Reynolds number regime of a turbulent wall plume, $(-\rho v)_{y\to\infty} = -\rho_\infty C_e u_m$, C_e is the entrainment constant, $u_m = au_1$, a is constant. According to the energy conservation and reaction enthalpy change formula (Liburdy and Faeth 1978):

$$r\,\dot{m}' = \frac{\dot{Q}'}{\Delta \mathrm{H}_{\mathrm{Ox}}} \tag{12}$$

where Q' is the energy release rate per unit wall width; $\Delta\mathrm{H}_{\mathrm{Ox}}$ is the reaction heat generated per unit mass of oxygen consumed, kJ/g.

According to Delichatsios and from Eq. (11) together with Eqs. (9), (10), (12) (Delichatsios 1984):

$$H = 4.65\left(\frac{\dot{Q}'}{c_p T_\infty \rho_\infty \sqrt{g}}\right)^{\frac{2}{3}} \tag{13}$$

Introduce the pine weathering coefficient to accurately assess the potential impacts of weathering on pyrolysis kinetics and flame stability. By quantifying this coefficient, we can characterize the changes in flame height during vertical flame spread scenarios. Combined with the weathering coefficient, the flame height can be expressed as:

$$H = 4.65\Pi\left(\frac{\mathrm{Q}'}{\mathrm{c_p T_\infty}\rho_\infty\sqrt{\mathrm{g}}}\right)^{\frac{2}{3}} \tag{14}$$

It can be assumed that the physical properties of the fuel are constant. Employing the properties shown in Table 3.

Figure 10 presents a comparative analysis of flame heights in weathered pine across different cycles. While the observed experimental values align with the theoretical model, which correlates the flame height with the energy release rate per unit wall width, they exhibit greater dispersion. In fluid turbulence, flame height arises from the balance between fuel pyrolysis and oxygen supply. Combustion energy is intrinsically linked to air entrainment from the boundary layer, rendering flame growth dependent on the intake of surrounding air. The buoyancy of hot gases generates upward flows that draw in fresh air through convection. By neglecting internal turbulence fluctuations and assuming a uniform distribution of radiative heat loss, with radiative heat flux proportional to the energy release rate, we can establish a linear relationship between flame height H and the energy release rate $\dot{Q}'$. The slope of this relationship reflects changes in the thermal properties of pine. With weathering coefficient adjustments, weathered pines demonstrate increased flame heights at equivalent energy release rates.

For vertical grain pine, the weathering coefficient rises quickly before stabilizing as the carbonized area and surface color difference increase. In contrast, horizontal grain pine exhibits gradual fluctuations in the carbonized area, resulting in a decline in the weathering coefficient. Consequently, during the middle and late stages of weathering, the weathering coefficient for transverse pine ranges from 50% to 61% of that for vertical grain pine. According to the experimental data presented in Figure 10, the flame height of weathered vertical grain pine is primarily concentrated in the region where $\dot{Q}' > 10$, peaking at $\dot{Q}' = 11$. In this case, the flame height typically exceeds 100 mm. This can be attributed to flame propagation aligned with the fiber direction, which enhances thermal conductivity, accelerates the release of volatile components, and facilitates

Table 3. Physical properties are used as the input for fire characteristics prediction.

Parameter		Quantity	Source
$Y_{\mathrm{Ox},\infty}$	Mass fraction of oxygen in the environment	23.22%	/
$\Delta\mathrm{H}_{\mathrm{Ox}}$	Reaction heat generated per unit mass of oxygen consumed	13kJ/g	/
ε	Mixing coefficient	6.6	(Hasemi 1984)
Pr	Prandtl number	0.7	(Liburdy and Faeth 1978)
C_f	Friction coefficient	0.015	(Liburdy and Faeth 1978)
C_e	Entrainment coefficient	0.0096	(Liburdy and Faeth 1978)

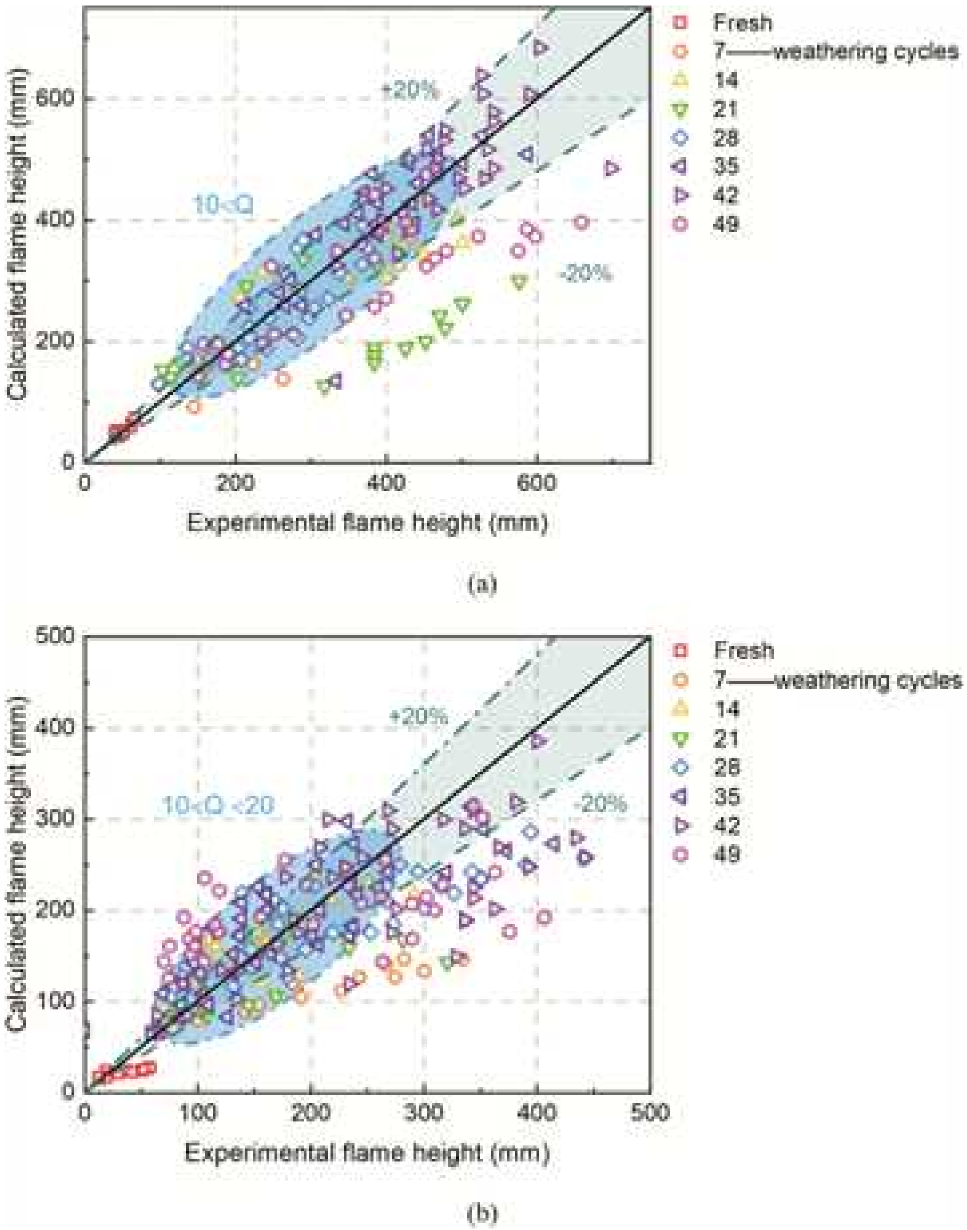

Figure 10. Comparison of the predicted and experimental flame height. (a) vertical grain pine. (b) horizontal grain pine.

swift heat diffusion along the axial direction. As a result, the flame maintains a relatively stable height while discharging significant energy. Conversely, the flame height of weathered horizontal grain pine falls within the range of 10 < $Q' < 20$. Although the height value distribution is broader here, it generally remains lower than that of vertical grain pine.

Previous studies have explored the correlation between flame height and energy release rate (Hasemi 1986; Tamanini 1977; Quintiere, Margaret and Hasemi 1986). The data shown in Figure 10 illustrates that the correlation proposed in this study exhibits higher prediction accuracy within the low energy release interval. However, as the energy release rate increases, the growth of flame height begins to slow and eventually stabilizes. Comparing the experimental and theoretical flame spread values for vertical and horizontal grain weathered pine reveals that the flame height of vertical grain pine increases rapidly in the medium and low energy regions, closely matching theoretical predictions. In the high-energy region, as the flame height reaches 120–130 mm, it flattens in response to energy release, causing experimental values to deviate from theoretical predictions. For weathered horizontal-grain pine, except for fresh wood, the experimental values align more closely with the linear progression of theoretical values. Notably, the flame height of the sample subjected to 49 cycles of weathering is slightly lower than the theoretical value.

On one hand, the weathering process leads to premature decomposition of surface components in the pine, reducing pyrolysis energy consumption, accelerating volatile matter release and enhancing the contribution of medium and low energy release rates to flame height, resulting in an approximately linear relationship. However, once a char layer forms, heat transfer through the pine is hindered, reducing pyrolysis efficiency and limiting flame height due to fuel energy availability. On the other hand, in the initial stage of combustion, weak air entrainment at low energy release rates, driven by buoyancy, results in oxygen primarily sustaining the combustion process, and the flame height increases gradually. In the medium energy region, as combustion reaches a relatively stable state, flame height exhibits slight fluctuations due to the linear relationship with energy release. However, in the high-energy region, turbulent pulsations intensify, the frequency of vortex shedding at the flame front increases, and oxygen mixing efficiency decreases, ultimately limiting flame extension. Consequently, the flame height exhibits a nonlinear relationship in this high-energy zone. In practical combustion processes, the linear relationship between fuel supply rate and energy release rate predicted by theoretical models may not hold in certain local areas. This is due to the formation and expansion of the char layer and variations in volatile matter release rates. Additionally, material anisotropy, as indicated by the changes in pine grain, further amplifies the effects of oxygen penetration and variations in thermal conductivity, contributing to discrepancies between theoretical predictions and experimental results.

4.4. Heat flux to the wall surface

The combustion characteristics of wall flames differ significantly from those of free flames, primarily due to the presence of radiative heat flux on most sample surfaces, which is a key factor influencing the combustion rate. Given the intermittent nature of the flame, it is hypothesized that radiation dominates the heat transfer process. When the sample remains unignited, the burner heat flux is measured at 20 kW/m^2. This study analyzes the flame reaction zone using the idealized linear fire source wall flame model developed by Quintiere and assumes the flame has a relatively thin optical thickness (Quintiere, Margaret, and Hasemi 1986). From the oxygen consumption rate, the energy release rate can then be determined:

$$\int_0^\infty \dot{q}'''dy = -\frac{(\rho v)_{y\to\infty}\cdot Y_{\mathrm{Ox},\infty}}{\varepsilon r}\Delta\mathrm{H} = -(\rho \mathrm{v})_{\mathrm{y}\to\infty}\frac{\mathrm{Y}_{\mathrm{Ox},\infty}\Delta\mathrm{H}_{\mathrm{Ox}}}{\varepsilon} \tag{15}$$

where ΔH is the reaction heat per unit mass of fuel, kJ/g.

Following Tamanini's wall flame model (Tamanini 1979), radiative heat flux q_r is proportional to energy release:

$$2\,\dot{q_{w,r''}} = \dot{q_r}'' = X_r\int_0^a \dot{q}'''dy \tag{16}$$

To satisfy the boundary conditions, the values of the profile function are (Quintiere, Margaret, and Hasemi 1986, 1986):

$$F(\eta) = \eta^{\frac{1}{7}}(1-\eta) \tag{17}$$

$$G(\eta) = \eta(1-\eta)^2 \tag{18}$$

when $\eta = 0$, $u = \theta = 1$; $\eta = 1$, $u = \theta = \frac{\partial\theta}{\partial\eta} = 0$; and when u near the wall, $\frac{1}{7}$ power holds $a = \frac{7}{8^{\frac{8}{7}}} = 0.650$ and $b = \frac{4}{27} = 0.148$:

$$\delta_0 = 1.06C_\mathrm{e} \tag{19}$$

$$\theta_0 = \frac{1.99a\theta_\mathrm{f}C_\mathrm{e}}{0.408aC_\mathrm{e} + abC_\mathrm{f}(Pr)^{-\frac{3}{2}}} \tag{20}$$

where $\theta_\mathrm{f} \equiv Y_{\mathrm{Ox},\infty}\frac{\Delta\mathrm{H}_{\mathrm{Ox}}(1-\mathrm{X}_\mathrm{r})}{\varepsilon c_\mathrm{p}}$. From Eqs.(15), (16), (17), (9) and (10):

$$\dot{q_{w,r''}} = \frac{0.306\rho_\infty Y_{Ox,\infty}\Delta\mathrm{H}_{\mathrm{Ox}}\mathrm{X}_\mathrm{r}\mathrm{u}_0\delta_0\mathrm{x}^{\frac{1}{2}}}{\varepsilon} \tag{21}$$

While convective flux $\dot{q_{w,c''}}$ follows Stanton number relations (Liburdy and Faeth 1978), where C_f is the friction coefficient, and St is the Stanton number, $St = \frac{1}{2}Pr^{-\frac{2}{3}}C_\mathrm{f}$:

$$\dot{q_{w,c''}} = St\left(\rho_\infty c_p u_m \theta_m\right) \tag{22}$$

The total heat flux simplifies to Eq.(23):

$$\dot{q_{w,c''}} = \frac{C_f}{2Pr^{\frac{2}{3}}}\rho_\infty c_p\theta_m = \frac{C_f}{2Pr^{\frac{2}{3}}}\rho_\infty c_p ab\theta_0 u_0 x^{\frac{1}{2}} \tag{23}$$

Normalize x using frame height and introduce the dimensionless term β. Combining the weathering coefficient Π, express $q_{w,c}''$ as:

$$\dot{q_w}'' = \dot{q_{w,r''}} + \dot{q_{w,c''}} = \rho_\infty u_0\left(\frac{0.306Y_{Ox,\infty}\Delta\mathrm{H}_{\mathrm{Ox}}\mathrm{X}_\mathrm{r}\mathrm{u}_0\delta_0}{\varepsilon} + \frac{abC_f c_p\theta_0}{2Pr^{\frac{2}{3}}}\right)x^{\frac{1}{2}} \tag{24}$$

$$\beta = \rho_{\infty} u_0 \left(\frac{0.306 Y_{Ox,\infty} \Delta \mathrm{H}_{\mathrm{Ox}} \mathrm{X}_{\mathrm{r}} \delta_0}{\varepsilon} + \frac{abC_f c_p \theta_0}{2Pr^{\frac{2}{3}}}\right) \left(\frac{1.5\varepsilon \dot{Q}'}{\rho_{\infty} Y_{Ox,\infty} \Delta \mathrm{H}_{\mathrm{Ox}} \mathrm{aC_e u_0}}\right)^{\frac{1}{3}} \tag{25}$$

Figure 11 shows the temporal variation of wall heat flux at five distinct heights along the center line of the pine during combustion. The data highlight a strong correlation between wall heat flux and combustion stages across various weathering cycles. For fresh pine, flame spread is predominantly driven by effective heat conduction along the grain, which allows heat to permeate quickly through the fibers and reach deeper areas, resulting in a relatively low overall surface heat flux. In the initial weathering stage, the degradation of fiber interactions and increased porosity lead to a peak flame heat flux of 27.5 to 30 kW/m^2. As weathering advances to the intermediate stage, the oxidation rate in the preheating zone rises. However, the expansion of pore areas and enhanced convection trap heat mainly at the lower surface of the pine, causing a reduction in peak intensity. In later weathering stages, the breakdown of conduction pathways within the wood decreases heat loss through conduction, allowing the peak heat flux to rise again, approaching 30 kW/m^2. When the pine is oriented perpendicular to the grain, the need for lateral heat penetration through the fiber layer increases resistance to heat conduction, resulting in a notable decline in flame heat flux compared to samples aligned with the grain. Analysis of heat flux at different heights reveals that the flame height remains stable below 0.54 m.

The interplay between weathering factors and wood grain influences the weathering process of pine, enhancing the release of volatile matter and prompting a transition from a diffusion flame to a premixed flame. Conversely, when wood is oriented perpendicular to the grain, inadequate oxygen supply can lead to localized accumulation of pyrolysis gas, resulting in intermittent combustion and increased fluctuations in heat flux. Pine aligned with the grain facilitates sustained combustion and extended flame duration due to a consistent and stable release of volatile matter, which contributes to a higher peak heat flux. In contrast,

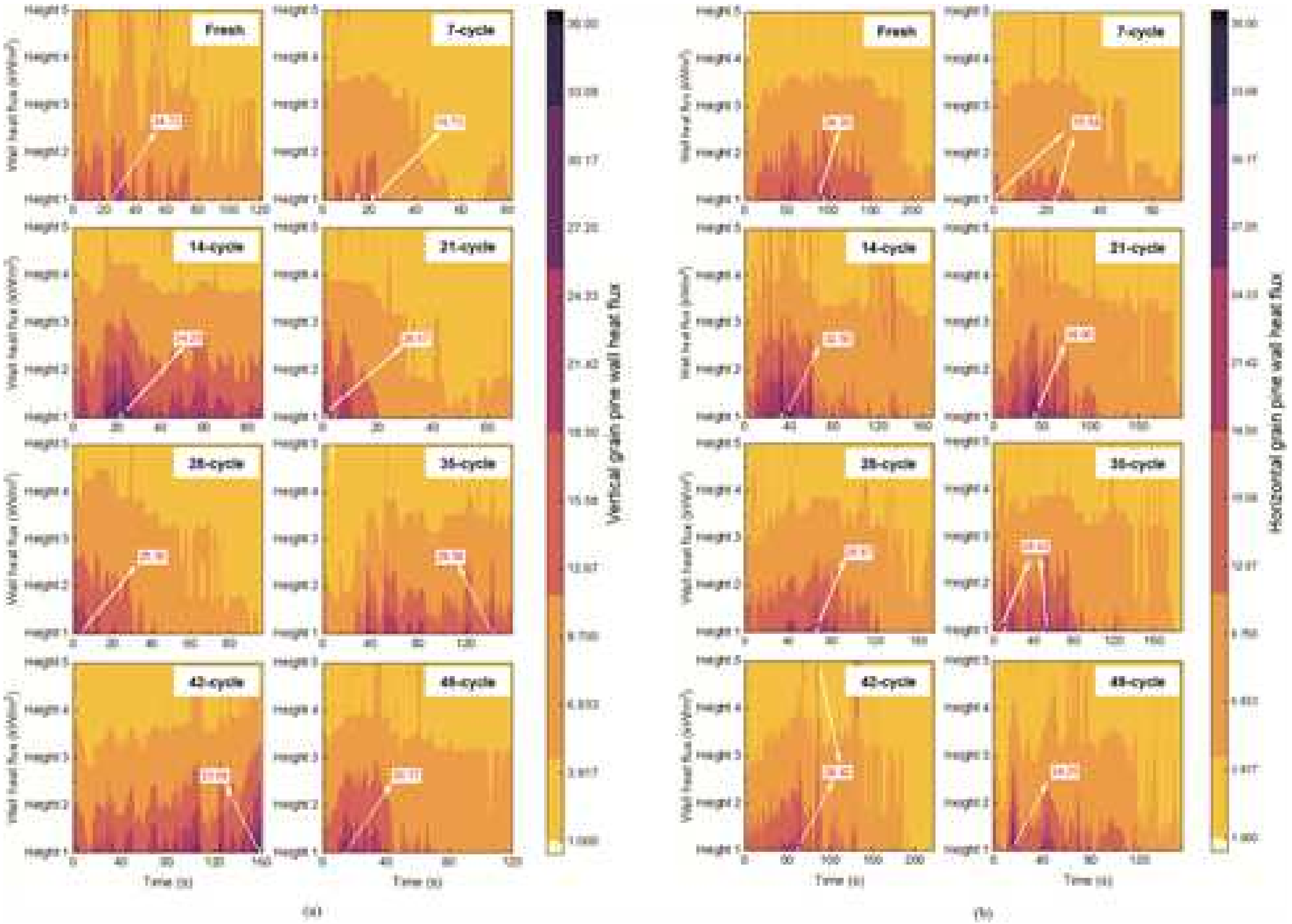

Figure 11. Wall heat flux on pine wall surfaces with varying wood grain patterns over time. (a) vertical grain pine wall heat flux (b) horizontal grain pine wall heat flux.

when positioned perpendicular to the grain, the combustion process is hindered as the release of volatile matter does not align with oxygen penetration. This results in a staged pyrolysis characterized by pulsed heat flux. Moreover, when a flame spreads vertically on pine aligned with the grain, the resulting carbonized layer is smooth and flat, enhancing heat emissivity and increasing heat flux. For pine oriented perpendicular to the grain, the flame alignment also positions itself perpendicularly, increasing energy loss and requiring additional heat to sustain combustion. Consequently, the overall heat flux value is reduced and becomes more stable.

Therefore, it can be found that in the flame reaction zone, the dependence of β is weak. q_w'' increases in proportion to $\left(\frac{x}{H}\right)^{\frac{1}{2}}$. In conjunction with Figure 4, the flame spread experiments reveal that as the vertical height increases, the wall heat flux gradually decreases. The peak heat flux measured ranges from 20 to 30 kW/m^2, with consistent heat flux levels observed in the combustion area. Consequently, scaling both the distance x and the flame height H to assess the wall heat flux distribution demonstrates considerable universality. Figure 12 illustrates the normalized height and total heat flux distribution for vertically spreading flames in both vertically and horizontally aligned weathered pine, with "EV" representing experimental values and "TV" indicating theoretical values. The observed discrepancies between these values can be attributed to several factors. First, the theoretical model does not account for the carbonization kinetics of pine or the diffusion limitations of oxygen in this porous medium. This oversight often results in experimental values that are lower than the theoretical predictions, particularly in regions of high wall heat flux. Second, the complexity of actual combustion involves numerous interrelated factors, including pine pyrolysis, chemical reactions on the surface and flame-fluid flow interactions. This intricacy challenges the theoretical model's ability to accurately assess flame propagation in pine. Moreover, while the assumption of relatively thin flame thickness suggests a diffusion-controlled regime, which depends on the mixing rate of fuel and oxygen, there is also a kinetic-controlled state influenced by the chemical reaction rate during combustion. The interaction between these regimes is dependent on the extent of premixing of volatile matter and oxidants, which is shaped by both the weathering cycle and wood grain orientation. It is also important to consider that experimental measurements of flame height are inherently subjective, and the measurement error associated with the heat flux meter can lead to a nonlinear distribution of the experimental values.

After linearly adjusting the weathering coefficient of the normalized flame height and considering the surface heterogeneity of pine, characterized by variations in grain and weathering effects, we find that accelerated degradation of cellulose and lignin increases porosity and crack propagation. These changes improve both oxygen permeability and combustion efficiency. In the low to medium heat flux ranges, the theoretical model aligns well with the experimental values of normalized flame height. However, in the high heat flux region, specifically when $q_w' > 10\,\mathrm{kW/m^2}$, the flame entrains a larger volume of surrounding air as it extends vertically. This process intensifies flame pulsation and turbulent mixing, leading to gradual stagnation and lateral expansion of the flame height. When comparing horizontal and vertical grain pine, the slope

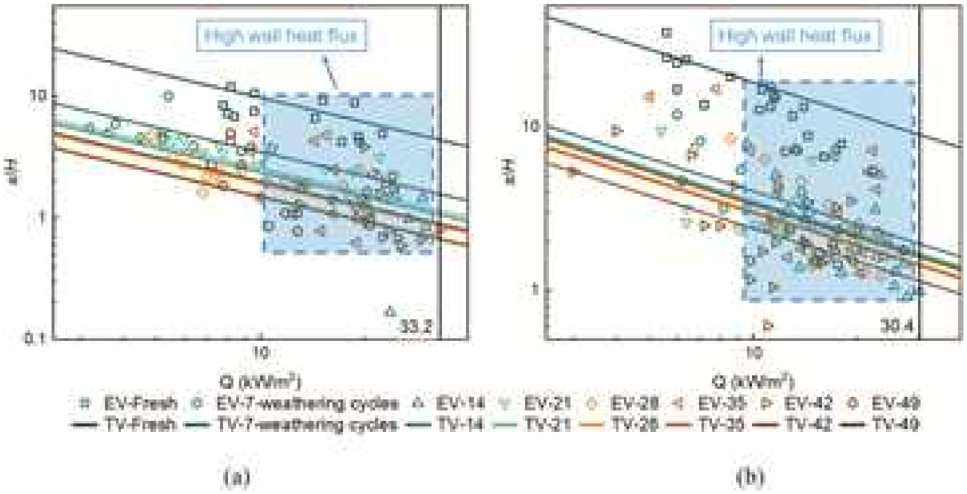

Figure 12. Normalized flame height and total heat flux distribution of the vertical spreading flame of pine. (a) vertical grain pine (b) horizontal grain pine.

of experimental values for horizontal grain is greater. Moreover, the normalized flame height exhibits a slight nonlinear plateau, indicating stagnation. This behavior is largely influenced by the impact of grain orientation on heat transfer pathways and variations in oxygen diffusion efficiency. The uneven lateral expansion of the charred layer in horizontal grain pine results in temperature variations along the vertical axis, which can inhibit surface pyrolysis while accelerating combustion reactions in localized areas. Consequently, this leads to a broader dispersion of experimental values for horizontal grain pine. Additionally, the theoretical model encounters difficulties in addressing the conditions associated with the lateral spread limitations of wood flames and the uneven carbonization of surfaces.

4.5. Upward flame spread rate

The flame spread rate is a critical parameter for evaluating fire development dynamics and quantifying the associated risks to ancient structures. While traditional quasi-static models effectively characterize the flame spread of wood by simplifying the continuous progression of the pyrolysis front, they fall short in accounting for the declines in spread rates resulting from fiber degradation and the structural compromises of weathered wood. To address this limitation, we introduce a weathering coefficient. This coefficient, in conjunction with considerations of weathering cycles and grain alterations, allows for a predictive model of flame spread rates in both vertical and horizontal weathered wood.

The position of the pyrolysis front is determined by the distance from the solid surface where the ignition temperature is reached, assuming that the flame spreads unidirectionally along the x-axis. One-dimensional heat conduction occurs at the solid surface, while the heat flux in the pyrolysis zone is moderated by the blocking effects of fuel gas injection and air entrainment at the wall surface. In this analysis, the dimensions along the × and y axes are treated as infinite. The system is categorized into three zones: the pyrolysis zone, the pyrolysis front and the preheating zone. By assuming gradual velocity changes over time, we can derive a formula for the flame spread velocity in the pyrolysis zone based on kinematic parameters. The velocity of the pyrolysis front can be approximated as follows:

$$V_\mathrm{p} = \frac{dx_\mathrm{p}}{dt} \cong \frac{x_\mathrm{p}(t+t_\mathrm{f}) - x_\mathrm{p}(t)}{t_\mathrm{f}} = \frac{x_\mathrm{f}(t) - x_\mathrm{p}(t)}{t_\mathrm{f}} \tag{26}$$

where x_p is the height of the pyrolysis front, mm; t_f is the time required for the pyrolysis front to pass through the flame heat exchange zone $x_\mathrm{f}(t) - x_\mathrm{p}(t)$. Therefore, when the initial surface temperature T_s is raised to T_ig through the constant heat flux of the wall $\dot{q_w}''$, $x_\mathrm{p}(t+t_\mathrm{f})$ is consistent with $x_\mathrm{f}(t)$. According to one-dimensional heat conduction theory, for a semi-infinite solid:

$$t_\mathrm{f} \cong k_\mathrm{s}\rho_\mathrm{s}c_\mathrm{s}\left(\frac{T_\mathrm{ig} - T_\mathrm{s}}{\dot{q}_{\mathrm{w}''}}\right)^2 \tag{27}$$

In addition, the surface temperature $T_\mathrm{w}(x,0)$ at the x can be expressed as:

$$T_\mathrm{w}(x,0) - T_\infty = \int_0^t \dot{q}_{\mathrm{w}''}(x, t-\tau)\cdot\emptyset(\tau)d\tau \tag{28}$$

where t and τ are time; $\emptyset(\tau)$ is the entrainment blocking effect on the wall surface under the condition of heat supply, $\emptyset(\tau) = \left(\pi\rho_\mathrm{s}c_\mathrm{s}\tau\right)^{-\frac{1}{2}}$:

$$\begin{aligned} T_\mathrm{ig} - T_\infty &= \int_0^t \dot{q}_{\mathrm{w}''}(x, t-\tau)\cdot\emptyset(\tau)d\tau \\ &= \int_0^x \frac{\dot{q}_{\mathrm{w}''}\left(x, \frac{x-x_\mathrm{p}}{V_\mathrm{p}}\right)}{\sqrt{\pi k_\mathrm{s}\rho_\mathrm{s}c_\mathrm{s}\left(x - x_\mathrm{p}\right)V_\mathrm{p}}}dx_\mathrm{p} \end{aligned} \tag{29}$$

where $\dot{q_w}''(x, t-\tau)$ depends on external radiation. Here, only the situation without external radiation considering flame propagation is considered. The incident heat flux is composed of flame radiation and convective heat flux.

Further assuming that the wall heat flux $\dot{q_w}''$ depends on the distance above the top of the pyrolysis zone; when the pyrolysis front is defined as δ_f, the asymptotic value of V_p is (Sibulkin et al. 1976):

$$V_p = \frac{\dot{q_w}''^2\delta_f}{\pi k_s\rho_s c_s\left(T_{ig} - T_\infty\right)^2} \tag{30}$$

The wall heat flux is influenced by flame radiation and is primarily affected by convection at the distal end of the wall. Flame height serves as a proportional factor in the distribution of wall heat transfer. In the turbulent free diffusion flame model, flame height is determined primarily by the heat release rate per unit length of pine and the deeper heat balance of the pine surface. During calculations, the temperature variable T_ig for weathered pine from Section 4.2 into the formula, using T_∞ set at 282.15 K. As the weathering coefficient increases with successive cycles, the flame spread time initially decreases before rising again with further weathering. By integrating the weathering coefficient with the weathering cycle and

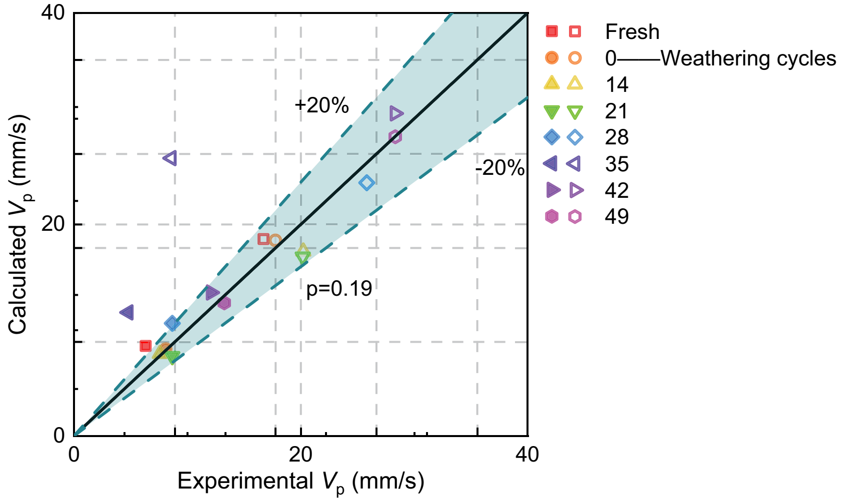

Figure 13. Comparison of calculated and experimental V_p of weathered pine with different grains.

wood grain properties to refine the prediction of the pine's flame spread rate:

$$V = \frac{V_p}{\Pi} = \frac{\frac{m}{m_0}}{\frac{d}{d_0}} \times \frac{S_0}{S_i} \times \frac{\dot{q}_{w''}{}^2 \delta_f}{\pi k_s \rho_s c_s \left(T_{ig} - T_\infty\right)^2} \tag{31}$$

Figure 13 shows the comparison of flame spread rates after correction by weathering coefficients between vertical and horizontal weathered pine and the experimentally measured flame spread rates. Solid patterns represent horizontal grain pine, while hollow patterns denote vertical grain pine. This model effectively predicts flame spread rates across different weathering cycles and wood grain orientations. According to the Wilcoxon signed-rank test, at $\alpha = 0.05$, shows no statistically significant difference between the experimental values and the calculated values. From the perspective of non-parametric tests, the overall alignment between the model's predicted values and the experimental data is quite favorable. Combined with the experimental phenomena, deviations in model predictions can be attributed to the presence of knots in the pine. Additionally, knots extend the time required for the pyrolysis zone to propagate to the top of the fuel, thereby reducing the actual flame spread rate. Overall, compared to fresh pine, the flame spread rate of weathered wood increases as the weathering cycle progresses. Empirical validation of Π's robustness is demonstrated across diverse aging conditions and anisotropic textures. As shown in Figure 13, Π maintains stable predictive capability for flame spread rates over 0–49 weathering cycles and both grain orientations. Comparatively, Zhou (Zhou et al. 2022) et al. incorporated grain direction but overlooked dynamic cycle-dependent changes.

5. Conclusions

This study examines the flame spread characteristics of vertical pine walls subjected to artificial weathering cycles and varying wood grain orientations. It examines the changes in flame behavior, including ignition temperature, flame height, heat flux and flame spread rate of weathered pine. A revised model for the flame spread rate was developed using the weathering coefficient and heat transfer analysis and validated against existing data. Key findings include:

(1) The study on weathered pine reveals that mass loss, shrinkage and morphology are closely linked to the number of weathering cycles. Mass loss continues with temperature and humidity changes, primarily occurring perpendicular to the grain, increasing risks of fracturing and warping. As cycles increase, the surface of the pine membrane may expand and detach.
(2) Flame spread on weathered pine varies by grain orientation. Vertical-grain wood shows slow horizontal flame progression but a larger carbonized area, while horizontal-grain wood allows for faster horizontal spread and slower vertical movement.
(3) In vertical flame spread, weathered pine displays distinct characteristics attributed to volatile content and pore conductivity, leading to higher temperatures and prolonged flame durations. Vertical-grain wood achieves slightly higher peak heat flux compared to horizontal-grain wood, which experiences low-frequency flame jitter.
(4) A weathering coefficient for pine has been established, integrating wood characteristics with fire

spread data, thereby enhancing predictive models for flame dynamics and aligning well with experimental results.

(5) For cycles ranging from 0 to 21, it is advisable to enhance the application of fire-retardant coatings. In contrast, for cycles exceeding 28, it is essential to prioritize structural reinforcement in response to flame acceleration driven by porosity factors.

The findings provide insights for fire risk assessment in heritage timber structures. Artificially accelerated weathering prevented isolating individual variables due to prioritizing holistic evaluation over mechanistic deconstruction to maintain weathering authenticity. The proposed Π coefficient assumes homogeneous material properties, indicating limitations in predicting heterogeneous combustion dynamics. Future work will focus on controlled single-variable weathering tests to quantify parameter-specific kinetics through integrated Arrhenius equation analyses, ensuring model robustness across diverse wood species and heritage conservation scenarios.

Disclosure statement

The authors declare that they have no known competing financial interests or personal relationships that could have appeared to influence the work reported in this paper.

Funding

This work was supported by the National Natural Science Foundation of China (No.52374248), the Beijing Nova Program (No.Z231100003823022), the Key-Area Research and Development Program of Guangdong Province (No.2024B1111080002), the Ordos key research and development program (No.YF20240026), Key Laboratory of Fire Protection Technology for Industry and Public Building Ministry of Emergency Management (No.2023KLIB02) and State Key Laboratory Cultivation Base for Gas Geology and Gas Control (Henan Polytechnic University) (No. WS2021A01).

CRediT authorship contribution statement

Kai Wang: Supervision, Resources, Project administration, Funding acquisition. **Danping Hao**: Writing—original draft, Visualization, Formal analysis. **Xuyao Wang**: Software, Investigation, Data curation. **Chenyang Jiang**: Writing—original draft, Methodology. **Yoshioka Hideki**: Writing—review & editing, Investigation. **Muying Ge**: Investigation. **Xuan Wang**: Validation, Supervision. **Biao Zhou**: Writing—review & editing, Project administration, Funding acquisition, Conceptualization.

References

Atreya, A., C. Carpentier, and M. Harkleroad. 1986. Effect of sample orientation on piloted ignition and flame spread. *Fire Safety Science* 1:97–109. doi: 10.3801/IAFSS.FSS.1-97.

Cetegen, B. M., and T. A. Ahmed. 1993. Experiments on the periodic instability of buoyant plumes and pool fires. *Combustion and Flame* 93 (1):157–84. doi: 10.1016/0010-2180(93)90090-P.

Chen, Y., Y. Hao, J. Wang, H. Gao, G. Liu, B. Lan, Y. Zhang, and J. Chen. 2023. Effect of ambient temperature and wind speed on horizontal flame spread and combustion trace on typical decorative wood boards. *Construction and Building Materials* 408:133597. doi: 10.1016/j.conbuildmat.2023.133597.

Delichatsios, M. 1984. Modeling of aircraft cabin fires. Gaithersburg, MD: National Institute of Standards and Technology.

Delichatsios, M. A. 1993. Transition from momentum to buoyancy-controlled turbulent jet diffusion flames and flame height relationships. *Combustion and Flame* 92 (4):349–64. doi: 10.1016/0010-2180(93)90148-V.

Di Blasi, C. 2008. Modeling chemical and physical processes of wood and biomass pyrolysis. *Progress in Energy and Combustion Science* 34 (1):47–90. doi: 10.1016/j.pecs.2006.12.001.

Gorbett, G. E., and S. P. Kozhumal. 2023. Fire fundamentals. In *Handbook of fire and the environment: impacts and mitigation*, edited by J. M. Brian, and M. McNamee, 55–100. Cham: Springer International Publishing.

Hartikainen, A., P. Yli-Pirilä, P. Tiitta, A. Leskinen, M. Kortelainen, J. Orasche, J. Schnelle-Kreis, K. E. J. Lehtinen, R. Zimmermann, J. Jokiniemi, et al. 2018. Volatile organic compounds from logwood combustion: Emissions and transformation under dark and photochemical aging conditions in a smog chamber. *Environmental Science and Technology* 52 (8):4979–88. doi: 10.1021/acs.est.7b06269.

Hasemi, Y. 1984. Experimental wall flame heat transfer correlations for the analysis of upward wall flame spread. *Fire Science and Technology* 4 (2):75–90. doi: 10.3210/fst.4.75.

Hasemi, Y. 1986. Thermal modeling of upward wall flame spread. *Fire Safety Science* 1:87–96. doi: 10.3801/IAFSS.FSS.1-87.

Herrera, R., A. Arrese, P. L. de Hoyos-Martinez, J. Labidi, and R. Llano-Ponte. 2018. Evolution of thermally modified wood properties exposed to natural and artificial weathering and its potential as an element for façades systems. *Construction and Building Materials* 172:233–42. doi: 10.1016/j.conbuildmat.2018.03.157.

Heskestad, G. 1998. On Q* and the dynamics of turbulent diffusion flames. *Fire Safety Journal* 30 (3):215–27. doi: 10.1016/S0379-7112(97)00035-0.

Heskestad, G. 1999. Turbulent jet diffusion flames: Consolidation of flame height data. *Combustion and Flame* 118 (1):51–60. doi: 10.1016/S0010-2180(98)00161-8 .

Heskestad, G., 2016. Fire Plumes, Flame Height, and Air Entrainment. In SFPE Handbook of Fire Protection Engineering, M. J. Hurley, 396–428. New York, NY: Springer. doi: 10.1007/978-1-4939-2565-0_13.

Hon, D. N. S., and W. C. Feist. 1986. Weathering characteristics of hardwood surfaces. *Wood Science and Technology* 20 (2):169–83. doi: 10.1007/BF00351028.

Hu, H., Z. Qi, J. Shi, H. Li, and J. Ji. 2024. Experimental and numerical investigations on fire development in a timber-based compartment with identification of characteristic events. *Journal of Building Engineering* 87:109033. doi: 10.1016/j.jobe.2024.109033.

Kránitz, K., W. Sonderegger, C.-T. Bues, and P. Niemz. 2016a. Effects of aging on wood: A literature review. *Wood Science and Technology* 50 (1):7–22. doi: 10.1007/s00226-015-0766-0.

Kránitz, K., W. Sonderegger, C.-T. Bues, and P. Niemz. 2016b. Effects of aging on wood: A literature review. *Wood Science and Technology* 50 (1):7–22. doi: 10.1007/s00226-015-0766-0.

Kropat, M., M. Hubbe, and P. Laleicke. 2020. Natural, accelerated, and simulated weathering of wood: A review. *Bioresources* 15 (4):9998–10062. doi: 10.15376/biores.15.4.Kropat.

Liburdy, J. A., and G. M. Faeth. 1978. Heat transfer and mean structure of a turbulent thermal plume along a vertical isothermal wall. *Journal of Heat Transfer* 100 (2):177–83. doi: 10.1115/1.3450777.

Ma, Y., L. Hu, Y. Huang, N. Zhu, and O. Fujita. 2021. Effect of sample thickness on concurrent steady spread behavior of floor- and ceiling flames. *Combustion and Flame* 233:111600. doi: 10.1016/j.combustflame.2021.111600.

Mackie, P., and F. Sim. 2019. Notre Dame de Paris. *Public Health* 170:A1–a2. doi: 10.1016/j.puhe.2019.04.009.

Morton, B. R., G. Taylor, and J. S. Turner. 1956. Turbulent gravitational convection from maintained and instantaneous sources. *Proceedings of the Royal Society of London Series A*, vol. 234, 1–23. doi: 10.1098/rspa.1956.0011.

Obataya, E. 2012. Recent progress in wood science around natural aging and artificial aging.

Popescu, C.-M., and A. Pfriem. 2020. Treatments and modification to improve the reaction to fire of wood and wood based products-an overview. *Fire and Materials* 44 (1):100–11. doi: 10.1002/fam.2779.

Quintiere, J., H. Margaret, and Y. Hasemi. 1986. Wall flames and implications for upward flame spread. *Combustion Science and Technology* 48 (3–4):191–222. doi: 10.1080/00102208608923893.

Rouse, H., C. S. Yih, and H. W. Humphreys. 1952. Gravitational convection from a boundary source. In *Tellus A. Dynamic Meteorology and Oceanography* 4 (3): 201–210. doi: 10.3402/tellusa.v4i3.8688.

Sá, D. M., M. R. Sá, and N. T. Lima. 2018. The National Museum and its role in the history of science and health in Brazil. *Cad Saude Publica* 34 (12):e00192818. doi: 10.1590/0102-311x00192818.

Schmidt, W. 1941. Turbulente ausbreitung eines stromes erhitzter luft. *Zamm-zeitschrift fur Angewandte Mathematik Und Mechanik* 21 (6):351–63. doi: 10.1002/zamm.19410210603.

Sibulkin, M., K. Jeongbin, V. Joseph, and J. Creeden. 1976. The dependence of flame propagation on surface heat transfer i. downward burning. *Combustion Science and Technology* 14 (1–3):43–56. doi: 10.1080/00102207608946745.

Song, J., J. Deng, J. Zhao, S. Lu, H. Ming, and C.-M. Shu. 2022. Comparative analysis of exothermic behaviour of fresh and aged pine wood. *Journal of Thermal Analysis and Calorimetry* 147 (24):14393–406. doi: 10.1007/s10973-022-11613-z.

Srinivas, K., and K. K. Pandey. 2012. Effect of heat treatment on color changes, dimensional stability, and mechanical properties of wood. *Journal of Wood Chemistry and Technology* 32 (4):304–16. doi: 10.1080/02773813.2012.674170.

Tamanini, F. 1977. Reaction rates, air entrainment and radiation in turbulent fire plumes. *Combustion and Flame* 30:85–101. doi: 10.1016/0010-2180(77)90053-0.

Tamanini, F. 1979. A numerical model for the prediction of radiation-controlled turbulent wall fires. *Symposium (International) on Combustion* 17 (1):1075–85. doi: 10.1016/S0082-0784(79)80103-4.

Tolvaj, L., and O. Faix. 1995. Artificial ageing of wood monitored by DRIFT spectroscopy and CIE L*a*b* color measurements. 1. effect of UV light. *Holzforschung* 49 (5):397–404.doi:10.1515/hfsg.1995.49.5.397.

Wang, K., D. Hao, B. Zhou, and C. Jiang. 2024. Research progress on influence mechanism of aging on wood combustion characteristics. *China Safety Science Journal* 34 (12):34–39. doi: 10.16265/j.cnki.issn1003-3033.2024.12.0083.

Xu, L., S. Li, W. Sun, X. Ma, and S. Cao. 2020. Combustion behaviors and characteristic parameters determination of sassafras wood under different heating conditions. *Energy* 203:117831. doi: 10.1016/j.energy.2020.117831.

Xu, L., X. Song, S. Li, J. Yu, Y. Qi, Y. Zhang, and X. Hong. 2024. Effect of different boundary conditions on the combustion properties and fire characteristics of typical woods. *Energy* 307:132696. doi: 10.1016/j.energy.2024.132696.

Yan, H. 2022. *Study on combustion and fire spread behaviors of typical wood structure buildings*. Doctor.

Yi, X., S. Lu, Y. Zhong, J. Zhang, and Y. Guo. 2024. Numerical simulation and safety assessment of fires in historic timber structures based on fire load investigation. *Heritage Science* 12 (1):222. doi: 10.1186/s40494-024-01344-9.

Zhou, B., C. Jiang, K. Wang, X. Romão, H. Yoshioka, W. Wang, Z. Tao, and H. Zhao. 2024. A review: The analysis of fires in Chinese historic building and research progress on the fire protection. *Thermal Science and Engineering Progress* 54:102850. doi: 10.1016/j.tsep.2024.102850.

Zhou, B., W. Kai, L. Yanyi, L. Yuhang, S. Xukun, Z. Feng, K. Wei, W. Xuan, Q. Bo, and Y. Han. 2022. Experimental study of upward flame spread over discrete weathered wood chips. *International Journal of Architectural Heritage* 16 (12):1797–808. doi: 10.1080/15583058.2021.1908446.

Zhou, B., K. Wang, W. Yang, W. Wang, B. Sun, M. Xu, X. Wang, and W. Ke. 2021. Influence of woodgrain orientation on the upward flame spread over discrete wood chips. *Case Studies in Thermal Engineering* 28:101616. doi: 10.1016/j.csite.2021.101616.

Zhou, B., H. Yoshioka, T. Noguchi, X. Wang, and C. Chiu Lam. 2019. Experimental study on fire performance of weathered cedar. *International Journal of Architectural Heritage* 13 (8):1195–208. doi: 10.1080/15583058.2018.1501115.

Zhou, Y., P. Zhou, R. Bu, X. Zhang, T. Chu, and Z. Wang. 2024. Horizontal flame spread behavior of densified wood: Effect of structural characteristics. *Fuel* 362:130687. doi: 10.1016/j.fuel.2023.130687.

Žlahtič Zupanc, M., and M. Humar. 2016. Influence of artificial and natural weathering on the hydrophobicity and surface properties of wood. *Bioresources* 11 (2):4964–89. doi: 10.15376/biores.11.2.4964-4989.